Electrochimica Acta 405 (2022) 139771

Contents lists available at ScienceDirect

Electrochimica Acta

journal homepage: www.elsevier.com/locate/electacta

Hydrodynamic interventions and measurement protocols to quantify and mitigate power overshoot in microbial fuel cells using microfluidics

Mehran Abbaszadeh Amirdehi[a], Lingling Gong[a], Nastaran Khodaparastasgarabad[a], Jayesh M. Sonawane[a], Bruce E. Logan[b], Jesse Greener[a,c,*]

[a] Département de Chimie, Faculté des sciences et de génie, Université Laval, 1045, avenue de la médecine, local, Québec City, QC G1V0A6, Canada.
[b] Department of Civil and Environmental Engineering, The Pennsylvania State University, University Park, PA 16802, United States.
[c] CHU de Québec, Centre de recherche, Université Laval, 10 rue de l'Espinay, Québec, QC, Canada.

ARTICLE INFO

Article history:
Received 27 August 2021
Revised 18 December 2021
Accepted 19 December 2021
Available online 20 December 2021

Keywords:
Microfluidics microbial fuel cells
Power overshoot
Power density curves
Geobacter sulfurreducens
Long-hold polarization test

ABSTRACT

Power overshoot in microbial fuel cells (MFCs) is an indicator of poor performance and its appearance in power density curves will hinder the determination of maximum power densities in continuously operating systems. In this work, a microfluidic approach was applied to an underperforming MFC containing a monoculture *Geobacter sulfurreducens* electroactive biofilm (EAB) to study power overshoot under idealized conditions. We developed an approach to quantify the degree of power overshoot while certain flow-based interventions were applied, notably shear erosion of the EAB outer layer. Two approaches to acclimation were also attempted. In the first, the MFC was acclimated to high currents before a standard polarization test. This eliminated the remaining overshoot behaviour and returned maximum power densities to pre-overshoot levels, though maximum current density remained low. In the second, a flow-assisted "long-hold polarization test" enabled full acclimation at each applied external resistance. Despite the underperforming state of the MFC, this method resulted in stable power and current density measurements that exceeded those made on the well-performing MFC using the standard polarization test. We conclude that slower electron transfer kinetics in the underperforming MFC can provoke overshoot, but a properly designed experiment that acquired polarization measurements using long-term acclimation at each external resistance overcame this problem.

1. Introduction

Microbial fuel cells (MFCs) are a high-priority sustainable-energy technology due to their ability to deliver usable current through an external circuit while simultaneously biodegrading organic molecules in waste streams or natural environments [1–3]. A polarization test is usually a key measurement, providing polarization curves (voltage versus current density) and power density curves (power density versus current density). One obtains maximum power output from a polarization test when the external and internal resistances are matched [2]. Alternatively, sacrificing power for operation at high current under a low external resistance could be a route to achieving high rates of substrate degradation. Regardless of the application, an ideal measurement would provide a reliable performance assessment during long-term MFC operation at any applied external resistance value.

Power overshoot is a common problem in MFCs linked to measurements obtained from electroactive biofilms (EABs) that have not stabilized to new conditions during polarization tests [4]. This overshoot (referred to as "type D") is characterized by tandem reductions in power and current when moving from low to high current densities in the power density curves, also known as "current double back". This is usually, but not exclusively, observed on the high current density side after the maximum power peak [5]. The presence of overshoot often correlates with the underestimation of power and current densities at some positions on the power density curve. A different type of overshoot (referred to as "type M") can result in artificially high power outputs [6,7]. No matter the type, overshoot is understood to inhibit accurate evaluations of maximum power and current. Overshoot can be reversibly triggered in well-performing MFCs by exposure to low nutrient concentrations, low ionic strengths, weak buffers, or low pH values [7,8], but in some underperforming MFCs, persistent overshoot can

* Corresponding author at: Département de Chimie, Faculté des sciences et de génie, Université Laval, 1045, avenue de la médecine, local, Québec City, QC G1V0A6, Canada.
E-mail address: jesse.greener@chm.ulaval.ca (J. Greener).

https://doi.org/10.1016/j.electacta.2021.139771
0013-4686/

occur even during exposure to ideal nutrient medium conditions. For example, the role of convection in overcoming diffusion limitations in nutrient delivery is usually not considered an important factor, but evidence is only based on persistent overshoot under stirring in batch MFCs [8]. Little is known about the origins of persistent overshoot, but given that it can exist under ideal conditions, some authors distinguish between MFCs that do not show current double back as "healthy" versus those which do as "overshooting" [7]. In this work we refer to well-performing and underperforming states, respectively.

Other than some interesting system-level control routines [9], the most generalized experimental strategy for dealing with overshoot is to acclimate the MFC to high current prior to a standard polarization test [10]. This approach (termed pre-acclimation in this work) provides time for the EAB to adapt, but it is not clear by which mechanism(s) the measured performance is improved or why the effect is only temporary. In considering this question, a focus should be placed on the measurement methodology. Whether carried out by switching external resistors or by conducting linear sweep voltammetry, polarization tests are not always straightforward for MFCs because the time required to reach stable behaviour may be too long relative to the experiment, especially under the influence of certain EAB health states, which can result in anomalies in power density curves [10]. Unlike during continuous operation of the MFC at a given external resistance, the polarization test itself continuously perturbs the EAB away from steady-state. The result may be a slow approach to a long-term stability based on biological adaptation (gene transcription, growth, etc.). As such, measurements collected with standard polarization tests, which range from minutes to hours per external resistor, may not represent stable MFC operation at various external resistances in the long-term. For the purposes of discussion in this work, the resulting differences in power density curves obtained without achieving long-term stability, compared to those which do, are considered artifacts. Thus, we arrive at the problem of untangling the inherent long-term performance of the MFC at all applied resistors in the power density curve from the influence of standard polarization measurements.

In order to equip researchers with tools to address remaining fundamental questions about the factors contributing to power overshoot in MFCs, new measurement approaches will be required. These should ensure that the technique does not influence the results. Of specific interest is the role of the measurement in producing overshooting power density curves, and relatedly, the connection amongst acclimation, time to reach stability, and the measured performance. In designing an appropriate proof-of-concept study, EABs form pure-culture *G. sulfurreducens* could be ideal because it can simplify interpretation by eliminating fluctuations in interspecies populations present in mixed-species EABs[11] and by limiting electron transfer to direct mechanisms only [12,13]. Precise control over operational conditions is also required to accurately probe the overshoot effect and potentially cure it. Microfluidic microbial bioelectrochemical systems have been used to study the effect of flow rate, the chemical composition of the nutrient solution, and other experimental conditions on measurable performance indicators such as EAB electrical outputs, kinetic parameters, and EAB pH [14–17]. When applied to MFCs, certain efficiencies can be realized in a microfluidic format. These include reduced start-up time, ability to eliminate ion exchange membranes, optimization of biofilm formation and outputs, and efficient assaying via parallelization [18–22]. In addition to eliminating the concentration cycling that occurs in batch-fed MFCs, continuous-flow microfluidic cells can allow accurate simulations and manipulation of concentration gradients [23], thus presenting an opportunity to validate assumptions that flow and nutrient availability can impact overshoot. A microfluidic approach may also be used to manipulate the EAB via controlled application of a large range of shear stresses. Even though the absolute current and power outputs are small in microfluidic MFCs, current and power densities are comparable with bulk-scale systems. The recent availability of microfluidic MFCs featuring standard graphite electrode materials and improved anaerobic operation under bench-top conditions have further closed the gap in performance compared with bulk-scale MFCs, having recently led to reliable operation for over half a year [24]. This advancement provides the proper experimental timescale to conduct meaningful studies on mature MFCs. Much like the field of organ-on-a-chip, these devices can enable detailed studies of biological system sub-components under precise conditions. Specifically, here we use the same microfluidic MFC design [24] to finally study overshoot in mature MFCs vis-a-vis solution concentrations, convection and other related hydrodynamic effects. We conducted an analysis of the degree of overshoot following the application of different flow rates, including those high enough to cause shear erosion of the outer biofilm layers. EAB erosion cured some, but not all, of the anomalies in the power density curve. Pre-acclimation to a low external resistance was then applied before a standard polarization test, resulting in somewhat improved MFC performance. Finally, a new microfluidic-assisted long-hold polarization test for in-progress acclimation at all external resistances was conducted in order to obtain measurements that better represented MFC properties under continuous operation at all applied external resistances.

2. Materials and methods

2.1. Fluidic simulations and calculations

Calculations of shear stress were obtained from a closed-form calculation, assuming an empty channel [25]:

$$\tau = \eta\left[\frac{Q\lambda}{2AD_h}\right] \tag{1}$$

where the viscosity of water is η=8.90 × 10^{-4} Pa s, Q is the volumetric flow rate (converted to units of m^3 s^{-1}), A is the channel cross-sectional area (m^2), and D_h is the hydraulic diameter (m) of the channel. The latter is given as:

$$D_h = \frac{4A}{P} \tag{2}$$

where P is the cross-sectional perimeter length (m). From Eq. (1), λ is a unitless shape factor, which has the following form for a rectangular duct with height (h) and width (w) [25]:

$$\lambda = \frac{24}{[(1-0.351h/w)(1+h/w)]^2} \tag{3}$$

See Supplementary Materials for a separate spreadsheet with the calculation of shear stress for all flow regimes used in this paper. Details for computational simulations of the anolyte and catholyte co-flow properties and concentrations are also presented in the Supplementary Materials. Briefly, these simulations accounted for mass transfer by convection, diffusion, and ion mobility, and the EAB thickness was estimated and implemented in the model.

2.2. Electrochemical measurements

Voltage measurements across external resistors (R_{ext}) were recorded using a potentiostat (VersaSTAT 4, Princeton Applied Research, USA) while continuously flowing a side-by-side laminar co-flow anolyte and catholyte across each respective electrode. Standard polarization tests in this work monitored the electrical discharge versus time after cycling from OCV to R_{ext} (50% duty cycle).

The base cycling time was 60 min, which was sufficient to reach electrochemical stability. In practice, cycle times of up to 90 min were used for some low values of R_{ext} or where the electrochemical stability was otherwise slow to become established. Switching between OCV and R_{ext} at this time scale strongly limits any acclimation to the different applied R_{ext} values during the polarization tests (i.e., strongly suppressing any in-progress acclimation). To further limit acclimation during standard polarization tests, R_{ext} values were always scanned from highest (300 kΩ) to lowest resistance (3.5 kΩ). Reaching stable voltages during standard polarization tests marks a short-term (electrochemical) stability at each R_{ext} value. Achieving this level of stability marks an electrochemical equilibrium in the system which is the benchmark for an accurate polarization test. As biological responses to changing external resistors will occur on a longer time-scale, achieving long-term stability at each R_{ext} was enabled with a so-called "long-hold" polarization test, in which R_{ext} was applied for up to 15 h after switching from OCV. Long-hold polarization tests allowed full biological acclimation to occur at each position on the power density curve (i.e., via in-progress acclimation), providing results that represent the long-term MFC operation at every applied resistor. Whereas measurements obtained after the reactor has achieved stability in the short-term will accurately represent the properties of the MFC at the time of measurement, unless long-term stability has also been reached, those results will represent an indefinite biological adaption state. This will not accurately represent of the MFC output under continuous operation at each point on the power density curve, so such an experimental design is considered suboptimal. Therefore, at the expense of a longer measurement, results achieving long-term stability via long-hold polarization tests are considered to produce ideal results.

Independent of the polarization test type used (standard or long-hold), we converted the voltage drop (V) across R_{ext} to current I (A) using Ohm's law (V=IR_{ext}) and normalized by the solution-exposed anode area A (30 mm^2) to obtain the corresponding current densities $\bar{I}$ (A m^{-2}) and power densities $\bar{P}$ (W m^{-2}):

$$\bar{I} = \frac{I}{A} = \frac{V}{A \times R_{ext}} \tag{4}$$

$$\bar{P} = \bar{I} \cdot V = (I^2 \cdot Rext)/A \tag{5}$$

The V versus $\bar{I}$ plots (polarization curves) and $\bar{P}$ versus $\bar{I}$ plots (power density curves) were created using Eqs. (4) and (5), respectively.

The accepted definition of type D overshoot is a simultaneous reduction in both $\bar{P}$ and $\bar{I}$ when moving from high to low external resistance on a power density curve, i.e., when $\Delta\bar{P} < 0$ and $\Delta\bar{I} < 0$ occur between any consecutive data pairs in a power density curve. From Eq. (5), it is sufficient to note that $\Delta\bar{I} < 0$ meets this definition because $\Delta\bar{P}$ is then necessarily negative as well. Therefore, the simplest way to quantify type D overshoot is to measure the absolute overshoot with the parameter $\Delta\bar{I}_{OS}$ (A), which is a positive value in the presence of overshoot:

$$\Delta\bar{I}_{OS} = \bar{I}_{max} - \bar{I}_f \tag{6}$$

where $\bar{I}_{max}$ is the maximum current density measured during a polarization test, and $\bar{I}_f$ is the final current density obtained at the lowest applied external resistance. In other words, $\Delta\bar{I}_{OS}$ is the quantification of the measured current double back associated with type D overshoot. It should be noted that this measurement is dependant on the values of R_{ext} chosen for the polarization test. While $\Delta\bar{I}_{OS}$ should not be used for quantitative comparisons between studies using different polarization test methodologies (including the application of different external resistor values and/or ranges in a switched resistor experiment), it is useful for comparing between like measurements, such as those conducted in this work. We also define a unitless measurement parameter called the overshoot factor θ_{OS}, which ranges from 0 (no overshoot) to 1 (complete loss of current):

$$\theta_{OS} = \frac{\Delta\bar{I}_{OS}}{\bar{I}_{max}} = 1 - \frac{\bar{I}_f}{\bar{I}_{max}} \tag{7}$$

In this work, the overshoot factor is expressed as a percentage [Θ_{OS} (%) = θ_{OS} × 100%]. A power density curve with no overshoot has $\bar{I}_f$=$\bar{I}_{max}$ and both $\Delta\bar{I}_{OS}$=0 and Θ_{OS}=0. It should be noted that following certain interventions, overshoot in an underperforming MFC may be reduced to $\Delta\bar{I}_{OS}$=0 at which point further improvement in measurement protocol can only be observed via changes to $\bar{I}_{max}$ or $\bar{P}_{max}$.

2.3. Microfluidic MFC design and operation

Moulds used to create the microfluidic MFC were fabricated via photolithography using a laminated photoresist and graphite electrodes (Isomolded Graphite Plate, GraphiteStore.com Inc., USA). The membraneless MFC device contains electrodes that were positioned flush with the top PDMS wall in the popular side-by-side arrangement in a channel with dimensions of 12 mm (width) by 0.16 mm (height). Other details on microfabrication, device design and biological handling protocols can be found in the Supplementary Materials (Section S1) and in the literature [24].

For most of this work, the inoculum consisted of a subculture of *G. sulfurreducens* (wild type, strain PCA, ATCC® 51573) in a nutrient medium with 40 mM sodium fumarate as a soluble electron acceptor. *In situ* confocal fluorescence microscopy experiments were conducted on the MFC containing an EAB that was inoculated with a similar inoculum except for the *G. sulfurreducens* was a GFP expressing strain (gifted from the Lovely group, U. Massachusetts Amherst). The nutrient medium consisted of a 10 mM $NaC_2H_3O_2$ (sodium acetate) solution, a trace mineral supplement (10 mL/L) (ATCC® MD-TMS™), and a vitamin supplement (10 mL/L) (ATCC® MD-TMS™) in a sodium phosphate buffer (3.8 mM NaH_2PO_4, 30 mM $NaHCO_3$, 1.3 mM KCl, 28 mM NH_4Cl). No oxygen scavengers were used in this work. The MFC anode was inoculated with the subculture by syringe pump (PhD 2000, Harvard Apparatus, MA) at a flow rate of Q_a=0.5 mL h^{-1} for two hours. To promote growth of the EAB after the inoculation, the same solution was used except that it was sterile and contained no sodium fumarate. A pH 7.0 sodium phosphate buffer containing 30 mM $K_3Fe(CN)_6$ (ferricyanide) was used as the catholyte solution to ensure that the cathode kinetics did not contribute to overshoot. At every stage, the catholyte formed a co-flow with the anolyte (Q_c=Q_a=0.5 mL h^{-1}). The laboratory temperature was 23 ± 0.5 °C. Other details related to bacterial preparation are identical to those of previous studies [24]. The experiment was run under flow conditions sufficient to ensure minimal acetate removal so as not to impact the conversion kinetics.

2.4. Imaging

Following the experiment, scanning electron microscopy (SEM) was applied to the EAB. The pumping system was used to deliver a fixant before sample extraction. Scanning electron microscopy (SEM) was performed after the experiment was completed to observe the bacteria attached to the anode. In preparation, a fixation solution (2.5% glutaraldehyde in phosphate buffer) was admitted into the channel (Q_T=1 mL h^{-1}) for 2 h Then the electrode was carefully removed from the microfluidic device in an anaerobic enclosure. The EAB-coated anode was left exposed to the same fixation solution in a bath overnight and was transferred the next day to a solution with 1% osmium tetroxide for 1.5 h and rinsed in phosphate buffer. Finally, the sample was sequentially dehydrated

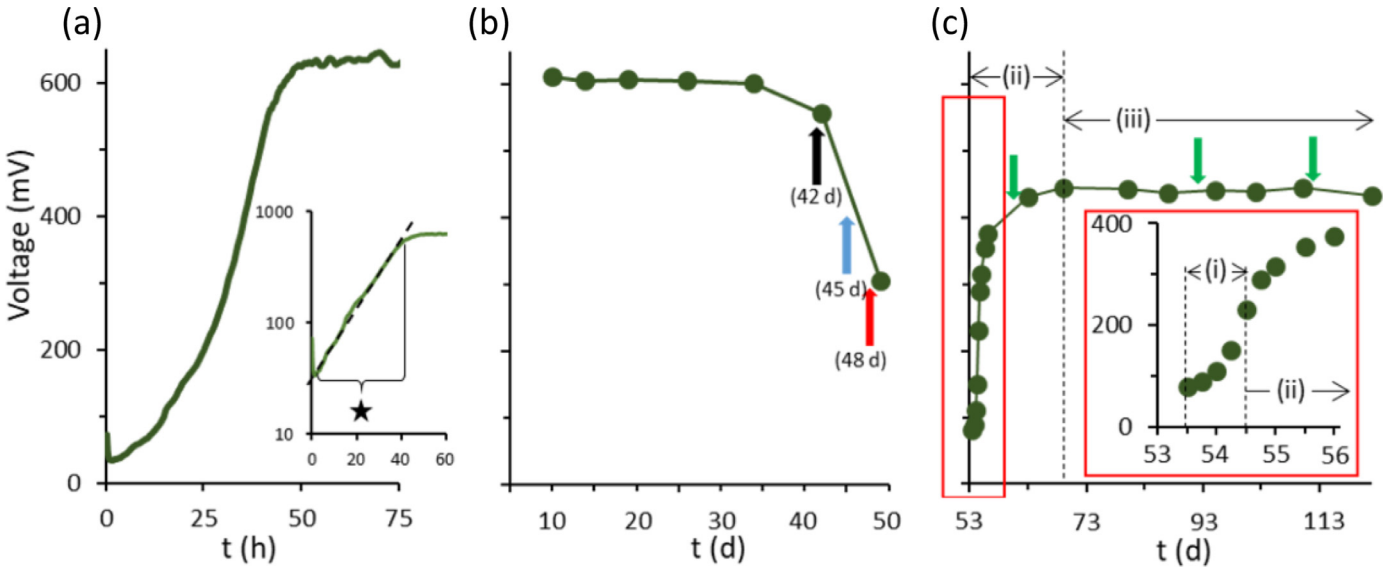

Fig. 1. (a) Voltage growth profile across external resistor R_{ext}=50 kΩ starting immediately after a 5 h inoculation process; inset shows semi-log plot of (a) with a highlighted section from 2 to 40 h (star) indicating the exponential growth period. (b) Voltage across R_{ext}=30 kΩ from intermittent voltage measurements between 5 and 50 days showing the onset of a reduction in voltage after approximately one month. Colour-coded arrows indicate the time at which the power density curves in Fig. 2 were obtained. (c) Voltage recovery starting 2 days after application of high shear force under external resistor R_{ext}=25 kΩ showing three recovery phases i, ii, and iii; inset shows zoom of (c) on the first three hours, displaying recovery during phase i. Arrows in (c) mark three time points (t = 61, 92 and 109 days) when power density and polarization curves were obtained. The time t = 0 starts after inoculation. Total flow rate (Q_T=1 mL h^{-1}) was generated from Q_a=Q_c=0.5 mL h^{-1} for (a), (b), and (c). The y-axis labels in (b) and (c) are shared with (a).

for 15 min in 50/50, 75/25, 95/5 and 100/0 ethanol/aqueous solutions and dried at room temperature overnight. A thin layer of gold was sputtered on the samples (Model: Nanotech, SEM PREP 2) before imaging with an electron microscope (JEOL JSM-6360 LV). More information is available in Supplementary Materials.

Confocal laser scanning microscopy (CLSM) (FV1200, Olympus, Japan) was used for the acquisition of 3D confocal stacks using a 50x (long-working distance) and 10x objectives. Detection was accomplished with a photomultiplier tube detector. The GFP expressing strain of *G. sulfurreducens* was excited at 488 nm and emission was detected in between 500–600 nm. Image stacks were analyzed using the Fiji bundle for ImageJ (National Institutes of Health, USA). Height measurement from CLSM 3D confocal stacks were achieved by determining the first and last slice where the biofilm was visible and in focus. More information is available in Supplementary Materials.

3. Results

3.1. Transition to an underperforming state and hydrodynamic interventions

We begin with a survey of the MFC voltage across the external resistor during the transition between the well-performing and underperforming states, followed by the results from the hydrodynamic interventions that were made. Almost immediately after inoculation, the voltage began to increase and continued exponentially for about 40 hours due to the growth of the EAB (Fig. 1a). After 3 days, the voltage became constant at 610 to 650 mV. At this time, the external resistor was reduced from R_{ext}=50 kΩ to 30 kΩ, and the MFC remained under flow conditions for 5 days until steady-state was reached. Afterwards, the voltage was recorded every 4–8 days (Fig. 1b), and standard polarization tests were conducted every week. The maximum power density remained relatively constant at $\tilde{P}_{max}$=370 mW m^{-2}, and no overshoot was observed (Supplementary Materials, Section S2).

At 42 days, the voltage across the 30 kΩ external resistor was slightly decreased and in days that followed it continued to drop, reaching 50% of its original value at t = 50 days. It is well-known that laminar flow in microchannels promote strong concentration gradients. Therefore, used simulations to investigate the possibility that the voltage loss occurred because some portions of the electrode experienced reduced activity due to local nutrient limitations (Supplementary Materials, Section S3). A simulation of the on-chip chemical concentrations showed that acetate was the most depleted at the downstream positions of the anode due to continuous consumption during the liquid transit across the upstream portions. Nevertheless, the concentration never fell below 9 mM at any position on the anode. As this is well above the concentration threshold between first- and zero-order kinetics (3–5 mM) [26,27], we conclude that access to substrate molecules was not a factor in the decreased cell voltage. A similar simulation showed that ferricyanide concentrations remained above 25.5 mM everywhere on the cathode, which is sufficient to avoid bottlenecks in reduction kinetics [28]. *In situ* microscopy was used to confirm that the EAB was stable, which indicates that the observed voltage loss was not due to EAB erosion. This is not surprising since the shear stress was only 4.8 × 10^{-3} Pa at these flow rates, which is well below values used in previous work where EABs could stability operate [23,29]. The microfluidic MFC was also designed to prevent O_2 contamination and ferricyanide crossover to the anolyte flow stream, but we do not rule out accidental contamination due to solution crossover during syringe replacement, from slow O_2 leaks through faults in the device gas-protection layer, fluid connects or even through the porous graphite electrodes. Other possibilities that could have led to the inhibited performance, include biological contamination and metabolically inactive outer layers, as recently reported [30].

We exploited the ability of the microfluidic MFC to apply a large range of shear stresses to investigate whether the outer layers comprized of older cells were the cause of the poor MFC performance. A large body of research is available which demonstrates and explains the phenomenon of biofilm erosion by shear

forces, both in traditional- and in microfluidic flow cells [31–33]. At t = 50 days, we applied a shear stress of approximately 143 Pa via three consecutive 3 s flow pulses (Q_a=Q_c=250 mL min^{-1}) to detach the EAB outer layers. Although no published data are available on critical shear stress thresholds for the erosion of *G. sulfurreducens* biofilms, these applied flow rates correspond to shear stresses that were more than 60 times higher than the highest reported shear stress for EAB erosion in other microfluidic MFCs [32]. After the high-shear flow pulses, a continuous high flow of Q_a=Q_c=8 mL min^{-1} (equivalent to 4.6 Pa) was applied for three minutes, and then the system was allowed to settle under a flow rate of Q_a=Q_c=0.5 mL h^{-1} (equivalent to 4.8 × 10^{-3} Pa) for two days. We conducted subsequent experiments on another membraneless MFC and verified that shear stresses as low as 0.6 Pa could reduce biomass by 50 percent (Supplementary Materials, Section S4). This confirms that the high shear stress (230 times higher) applied to the EAB after 50 days was enough to cause erosion. Upon resumption of measurements across the 25 kΩ external resistor (reduced from 30 kΩ to encourage biofilm re-growth after shear erosion), a non-zero voltage (80 mV) was observed (Fig. 1c). We believe that this signal was related to a remaining biofilm seed layer [33]. This hypothesis was based on a previous study on the same graphite electrode material in a microfluidic electrochemical impedance experiment which had confirmed residual quantities of a *Pseudomonas* biofilm were retained following shear erosion of the biofilm outer layers, possibly aided by the electrode surface roughness at the microscale. The voltage initially recovered to 225 mV approximately one day after the measurements were restarted (t = 53 days, marked as phase i in Fig. 1c), followed by a slow recovery over the next 20 days (phase ii), and finally, a steady-state potential of 450 mV was attained (phase iii). The initial current increase during phase i was likely due to the recovery of the biofilm metabolism after re-establishment of the initial co-flow conditions and washout of anolyte and catholyte solutions that may have crossed over to the opposite electrode compartment. The slower recovery in phase ii was likely due to biofilm regrowth from the residual *G. sulfurreducens* seed layer. When the MFC reached steady-state in phase iii (t = 61 days), the voltage was improved compared to t = 48 days, but remained lower than the pre-overshoot voltages (at t = 42 days). Accounting for the reduced external resistance of R_{ext}=25 kΩ at t = 61 days compared to R_{ext}=30 kΩ at t>48 days, the voltagewas reduced by 12% (calculated using Ohm's law) and power was reduced by 36% (calculated using Eq. (5)). Despite the EAB erosion following higher shear stresses, the current was approximately doubled and power increased by 330% compared to the output at t = 48 days.

3.2. Power density curves demonstrating overshoot

Next, the reduced MFC performance that occurred after t = 42 days was investigated by evaluating the power density curves Fig. 2). Standard polarization tests were conducted after the MFC potential began to drop (at 42 days), and the polarization and power density curves were generated according to Eqs. (4) and (5), respectively. The same cycling time regime as used here (approximately 60 min) was sufficient for a well-performing MFC of the same design to reach a stable value in the short-term [24]. Initially (t = 42 days), the power density curves showed a typical monotonic approach to maximum power density ($\bar{P}_{max}$=360 mW m^{-2}), and no overshoot was observed at high current densities, similar to measurements observed during the first month.

As the MFC performance became further degraded (after t = 45 days), two different anomalies were observed in the power density curves. The first was a precipitous reduction in $\bar{P}$ near the former apex of the power density curve (similar to type M overshoot), and the second was a classic current overshoot at low external loads,

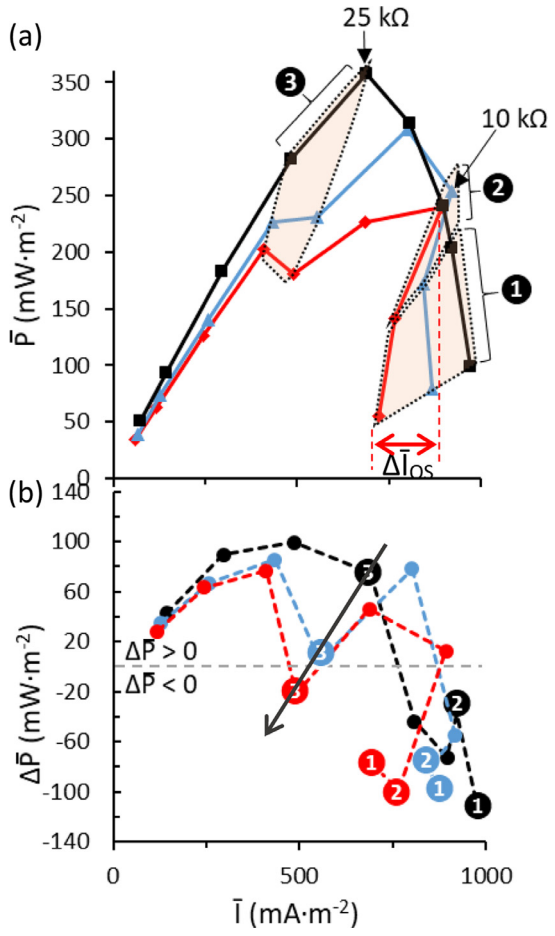

Fig. 2. Results from MFC polarization test and overshoot analysis during the transition from a well-performing state to an overshooting state. (a) Power density curves at t = 42 days (black), t = 45 days (red), and t = 48 days (blue). Based on the previously estimated internal resistance of 25 kΩ, the external resistors used were R_{ext}=300, 150, 70, 40, 25, 15, 10, 8, and 3.5 kΩ. Power densities measured at two critical external resistances (25 and 10 kΩ) are highlighted (black arrows). Absolute overshoot ($\Delta\bar{I}_{OS}$) is exemplified at t = 48 days with a horizontal arrow (red). (b) $\Delta\bar{P}$ versus $\bar{I}$ for the same data in (a). Data in (a) and (b) share the same colour coding and x-axis. Regions 1, 2 and 3 indicate data pairs in all three power density plots in (a) that correspond to $\Delta\bar{P}$ in (b).

R_{ext} < 10 kΩ (similar to type D overshoot). We consider these two phenomena separately and go beyond the usual definition of overshoot ($\Delta\bar{I}$ < 0, $\Delta\bar{P}$ < 0 in a power density curve) by quantifying the current double back using Eq. (6). At t = 45 days, the measured absolute overshoot was $\Delta\bar{I}_{OS}$=54 mA m^{-2}. According to Eq. (7), this is equivalent to an overshoot factor of Θ_{OS}=6%. At t = 48 days, the absolute overshoot more than tripled to $\Delta\bar{I}_{OS}$=173 mA m^{-2}, with a corresponding increase in the overshoot factor to Θ_{OS}=19%. This change signals a rapid decline in the MFC performance.

The second anomaly was the local drop in power density at the apex of the power density curve observed at t = 44, 45 and 48 days. A similar anomaly has been linked to polarization tests that are conducted too quickly, producing unpredictable power density readings [9]. This effect is usually accompanied by a corresponding reduction in current density at the same position, thus meeting the definition of type M overshoot [7]. Changes in $\bar{P}$ at 25 kΩ are shown in Fig. 2b in a $\Delta\bar{P}$ versus $\bar{I}$ curve and can be compared to the power density curve in Fig. 2a. Insofar as $\Delta\bar{P}$ and $\Delta\bar{I}$ determine the presence of power overshoot, we plot $\Delta\bar{P}$ versus $\Delta\bar{I}$ (Supplementary Materials, Section S4). It is clear that while $\bar{I}$ continuously increases (i.e., $\Delta\bar{I}$ > 0, always) even as $\Delta\bar{P}$ becomes negative near the former power density apex (R_{ext}=25 kΩ), the values of $\bar{I}$ at 25

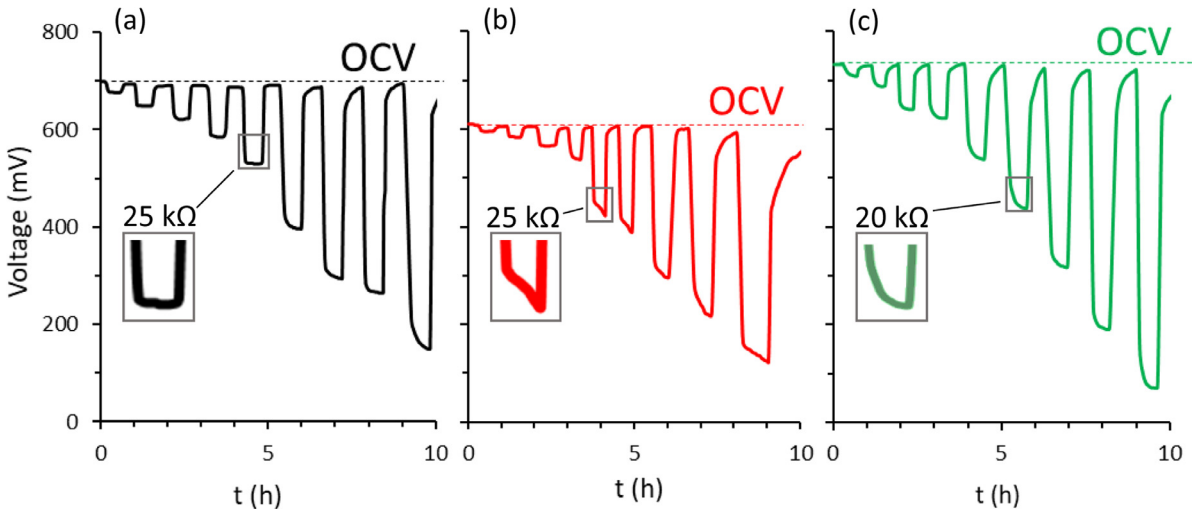

Fig. 3. Voltage versus time discharge profiles from polarization tests at t = 42 (before overshoot), 48 (during overshoot) and 61 days (three days following EAB erosion) are shown in (a), (b) and (c), respectively. Insets in each figure show a close-up view for a single transition from OCV to R_{ext}=25 kΩ in (a) and (b) and from OCV to R_{ext}=20 kΩ (c). Resistor values used in (a) and (b) were R_{ext}=300, 150, 70, 40, 25, 15, 10, 8, and 3.5 kΩ. Resistor values in (c) were R_{ext}=300, 150, 80, 50, 30, 20, 15, 8, and 3.5 kΩ. The y-axis labels and voltage range in (b) and (c) are the same as in (a).

kΩ and $\Delta\bar{I}$ between 40 and 25 kΩ are both progressively reduced with time. From these trends, it appears that further degradation of the MFC performance could have resulted in $\Delta\bar{I} < 0$ (classic type M overshoot) for the data pair marked 3 in Fig. 2a, similar to the data pairs marked 1 and 2. It should be noted that calculations for $\Delta\bar{I}$ and $\Delta\bar{P}$ should be taken as qualitative and only considered to show general trends since they consider consecutive resistances, which are not separated by the same increment.

3.3. The role of polarization test stability in measurements featuring power overshoot

We hypothesized that the anomalies observed in the power density curves in Fig. 2 were correlated to slow electron transfer as concluded previously [7]. We inspected the raw voltage versus time discharge profiles generated during the standard switched resistor polarization tests. At t = 42 days (before overshoot), a rapid exponential approach to stable values occurred during discharge from OCV across each of the connected external resistors except for R_{ext}=3.5 kΩ, where the system was still discharging before the voltage was recorded (Fig. 3a). In contrast, discharge profiles were often irregular and incomplete (i.e., not electrochemically stable) during the standard polarization tests acquired at t = 45 and 48 days (during overshoot) at values of R_{ext} lower than 100 kΩ (e.g., Fig. 3b at t = 48 days). This information is shown in greater detail in the inset to Fig. 3a and 3b for the discharge across the 25 kΩ external resistor. Based on the discharge profiles, the local decrease in the power density curve at R_{ext}=25 kΩ and the overshoot at R_{ext} < 10 kΩ could have been artifacts related to worsening electron transfer kinetics. That is, due to slower electron transfer, hold times were no longer sufficient to achieve short-term stability during standard polarization tests. This supports previous studies showing that worsening electron transfer kinetics at the bioanode is linked to similar behaviour [4,7,34]. It is out of the scope of this work to pinpoint the cause of the worsening electron transfer at play in the transition to the MFC overshooting state, but some possibilities include changes in charge transfer components [35], including: number of bacteria, changes to the number and types of cytochrome c proteins and conductive pili (per bacterium) [36], bioanode capacitance [37], electrical resistance of the bulk biofilm, [38,39] or charge transfer resistance from the EAB to the electrode [26]. Coincident with the observed slower electron transfer kinetics at t = 48 days was a reduction in OCV by approximately 50 mV compared to t = 42 days (Fig. 3a and 3b). Loss of OCV could be the result of a loss of cytochrome c charge carriers or a reduced EAB metabolism.

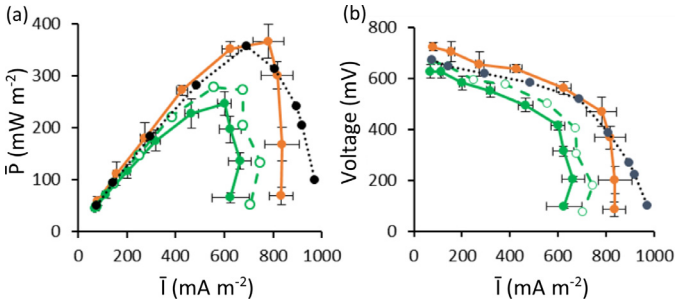

Fig. 4. Power density curves (a) and polarization curves (b) obtained at different times and conditions. In both figures, the performance before the onset of overshooting behaviour is reproduced from Fig. 2a as a reference (t = 42 days, black dotted curve). Average results after shear erosion at total flow rate Q_T=1 mL h^{-1} are shown (t = 61, 92, 109 days, green solid curve); results after an increase of total flow rate to Q_T=10 mL h^{-1} (t = 110 d, green dashed curve); and average results after 4 days of pre-acclimation at R_{ext}=3.5 kΩ at flow rate Q_T=1 mL h^{-1} are shown with error bars (t = 115 to 120 days, orange). All error bars are the result of 3 separate measurements on different days.

We also examined the discharge profiles after erosion of the outer EAB layers (e.g., Fig. 3c at t = 61 days). Data were representative of measurements at t = 92 and 109 days (data not shown). It is also noted that the polarization curves (Supplementary Materials, Section S5) did not show significant differences in slope in the ohmic region after 61 days, indicating that the internal resistance was also stable in this time period. The discharge profiles returned to an exponential decay, and short-term stability was reached more often before switching back to OCV in the cycle time (60 to 90 min) under a standard polarization test. We conclude that removal of the outer EAB layers resulted in improved electron transfer kinetics and rendered the polarization test valid by enabling the electrochemical (short-term) stability criterion to be met. Likely related to this was the disappearance of the anomalous power loss at 25 kΩ in the corresponding power density curve (Fig. 4). However, overshoot was still observed at low external loads (R_{ext} < 8 kΩ). The average absolute overshoot be-

tween t = 61 and t = 109 days was measured as $\Delta\bar{I}_{OS}$=88.7 ± 7.1 mA m^2 (with the corresponding average overshoot factor of Θ_{OS}=13 ± 2%), which is a reduction from the overshoot at t = 48 days ($\Delta\bar{I}_{OS}$=173 mA m^2, Θ_{OS}=19%). Despite these improvements, it is noted that the $\bar{I}_{max}$ after shear erosion was lower (663 mA m^{-2}) than was observed while overshoot was present and most severe (723 mA m^{-2}). This is consistent with reduced biomass after erosion, but the internal resistance also appeared to be higher after erosion compared to before overshoot onset (Supplementary Materials, Section S5). Taken together, shear erosion made some improvements in the MFC performance, but it is clear that the MFC was still underperforming compared to the pre-overshoot state.

We tested the hypothesis that moderate (sub-erosion) increases to flow and the related reductions in diffusion barriers could reduce or even eliminate $\Delta\bar{I}_{OS}$ because overshoot is situated in the concentration-limited regime of the polarization curve. We limited the maximum flow rate to Q_T=10 mL h^{-1} because this only represented a shear stress of 4.8 × 10^{-2} Pa is lower than other reported *G. Sulfurreducens* studies and because beyond this value the returns on the MFC output are diminishing [24]. In addition to an expected increase in $\bar{P}_{max}$ and $\bar{I}_{max}$ (Fig. 4), the increased flow rate reduced the absolute overshoot to $\Delta\bar{I}_{OS}$=40 mA m^{-2} (with a corresponding overshoot factor of Θ_{OS}=5%). Inspection of the corresponding polarization curve indicated a small reduction (5 kΩ) in the internal resistance over the value obtained at Q_T=1 mL h^{-1} (36 kΩ) (Supplementary Materials, Section S5). This was corroborated by the calculated internal resistance (not shown) [2]. This is contrasted by previous measurements in a two-chamber *G. sulfurreducens* MFC with continuous anolyte replacement, whereby higher internal resistances and lower power were measured at high flow rates [40], which may have reflected amplified stresses, e.g., those due to flow-enhanced transport of low concentration O_2 in solution to the EAB, as other literature examples typically show an increase to power with the flow [29,41].

3.4. Pre-acclimation to a low external resistance

The second half of the study focused on testing the effects of different acclimation methods. These included acclimation to high current conditions via a low R_{ext} (3.5 kΩ) before standard polarization tests (pre-acclimation) or resistor-specific acclimation during microfluidic-assisted long-hold polarization tests (which we call in-progress acclimation). In the first approach, the MFC was pre-acclimated at 3.5 kΩ for 4 days. In the literature, pre-acclimation is normally performed with a low external resistor to extract improvements in MFC performance. In this work, in addition to applying pre-acclimation to 3.5 kΩ (low by microfluidic MFC standards), we applied two other resistor values (R_{ext}=150 and 20 kΩ) to demonstrate the relationship between holding at (i.e., pre-acclimating to) high resistances and the reduced MFC performance under standard a polarization test. Each of these pre-acclimation resistanges was applied three times in random order to prevent bias in the results, while the polarization test in each case was conduced normally, by applying R_{ext} from high to low values. Pre-acclimation at the lowest external resistor (R_{ext}=3.5 kΩ) was most efficient in improving outputs. Specifically, $\bar{P}_{max}$ recovered to pre-overshoot levels ($\bar{P}_{max}$=370 mW m^{-2}), and the overshoot was eliminated ($\bar{I}_f$=$\bar{I}_{max}$). However, the $\bar{I}_{max}$ value of 810 mA m^{-2} after pre-acclimation was still 20% lower than that at t = 42 days (before the onset of overshoot) and was nearly equivalent to $\bar{I}_{max}$ at t = 45 and 48 days (during overshoot). We do not believe that this low current relative to pre-overshoot values is the same as has been reported during MFC start-up [42] because in this case, the drop in current was relative to an already mature MFC. Rather, it is likely the result of the continued EAB underperformance and of loss of biomass after shear erosion [43]. For comparison, we combine the pre-acclimated power density and polarization curves along with those data obtained at t = 42 days in Fig. 4. Pre-acclimation to higher resistances had the predictable effect of lowering $\bar{P}_{max}$ and $\bar{I}_{max}$ [9], and commensurate increases in internal resistance were observed (Supplementary Materials Section S7).

3.5. In-progress acclimation via flow-assisted long-hold polarization tests

The beneficial effects of pre-acclimation to a single low external resistor before a standard polarization test might be partially reversed while the EAB readapts to higher loads during the measurement. As well, the relatively rapid cycle time between OCV and R_{ext} is too short to achieve long-term (biological) stability related to bacterial adaption to different currents during the polarization test. Another approach is in-progress acclimation in which the polarization at each R_{ext} is held for a long duration so that every point in the power density curve is fully and individually acclimated, thus achieving long-term stability. The accurate and constant flow from the microfluidic MFC eliminates nutrient cycling and the related voltage cycling that occurs in batch MFCs. Thus, microfluidic MFCs can provide a unique perspective on acclimation dynamics at each resistor in a polarization test. We acquired the discharge curves during long-hold polarization tests with dwell times of up to 15 h following the switch from OCV to selected R_{ext} values, and each measurement was repeated three times at two different flow rates (Q_T=1 and 10 mL h^{-1}). In all cases, the voltage stabilized at a minimum value over a relatively short timescale (termed t_s'). For R_{ext} < 50 kΩ, the voltage was observed to eventually increase to a new (acclimated) voltage in a long time-scale stabilization (termed t_s''). This time to adjust to high current demand is probably due to the same effect involved in the so-called current recovery observed sometimes in the power density curves near the end of the experiment [40]. Both t_s' and t_s'' increased with decreasing R_{ext}, but interestingly, applying higher flow rates reduced these times. As an example, Fig. 5a–c below show three discharge curves across external resistances of R_{ext}=3.5, 30, and 300 kΩ. A plot of the measured t_s'' as a function of R_{ext} under low- and high flow rates (Fig. 5d) shows that the acclimation times were 6 to 11 h at Q_T=1 mL h^{-1} but were only 4 to 7 h at Q_T=10 mL h^{-1}. Thus, in addition to achieving acclimation under well-defined concentrations (e.g., no concentration cycling), we estimate that the flow-assisted long-hold approach provides the benefit of a 4.5- to 18-times reduction in experimental time using compared to multi-cycle acclimation over three fill/deplete cycles per external resistor in a bulk MFC [10]. We believe that studies focused on the degree and timing of the voltage recovery can provide insights into the specific nature of the biological process(es) that occur in response to acclimation, e.g., biofilm growth, cytochrome or other protein expression, and shifts in metabolic states, amongst other factors.

We constructed power density and polarization curves (Fig. 5e and 5f) from long-hold polarization tests based on the voltages obtained after "virtual hold times", t_s' and t_s'', each repeated for flow rates Q_T=1 and 10 mL h^{-1}. In all cases, $\bar{P}_{max}$ was obtained at R_{ext}=20 kΩ. At Q_T=1 mL h^{-1}, the $\bar{P}_{max}$ value after hold time t_s' was 346 mW m^{-2} (slightly lower but within the standard deviation of the average value (370 mW m^{-2}) obtained from a standard polarization test following constant acclimation to 3.5 kΩ). This value increased to 383 mW m^{-2} under flow rate Q_T=10 mL h^{-1}. At hold times of t_s', absolute overshoot persisted, with $\Delta\bar{I}_{OS}$=205 (and the corresponding overshoot factor of Θ_{OS}=24.5%) at Q_T=1 mL h^{-1} and 74 mA m^{-2} (Θ_{OS}=8.5%) at 10 mL h^{-1}. In contrast, the overshoot was fully eliminated for power density curves that were constructed using voltages at t = t_s'' from the polarization test voltage versus time profiles. In addition, $\bar{P}_{max}$ and $\bar{I}_{max}$ were improved ($\bar{P}_{max}$=405 mW m^{-2} and $\bar{I}_{max}$=1038 mA m^{-2} at Q_T=1 mL

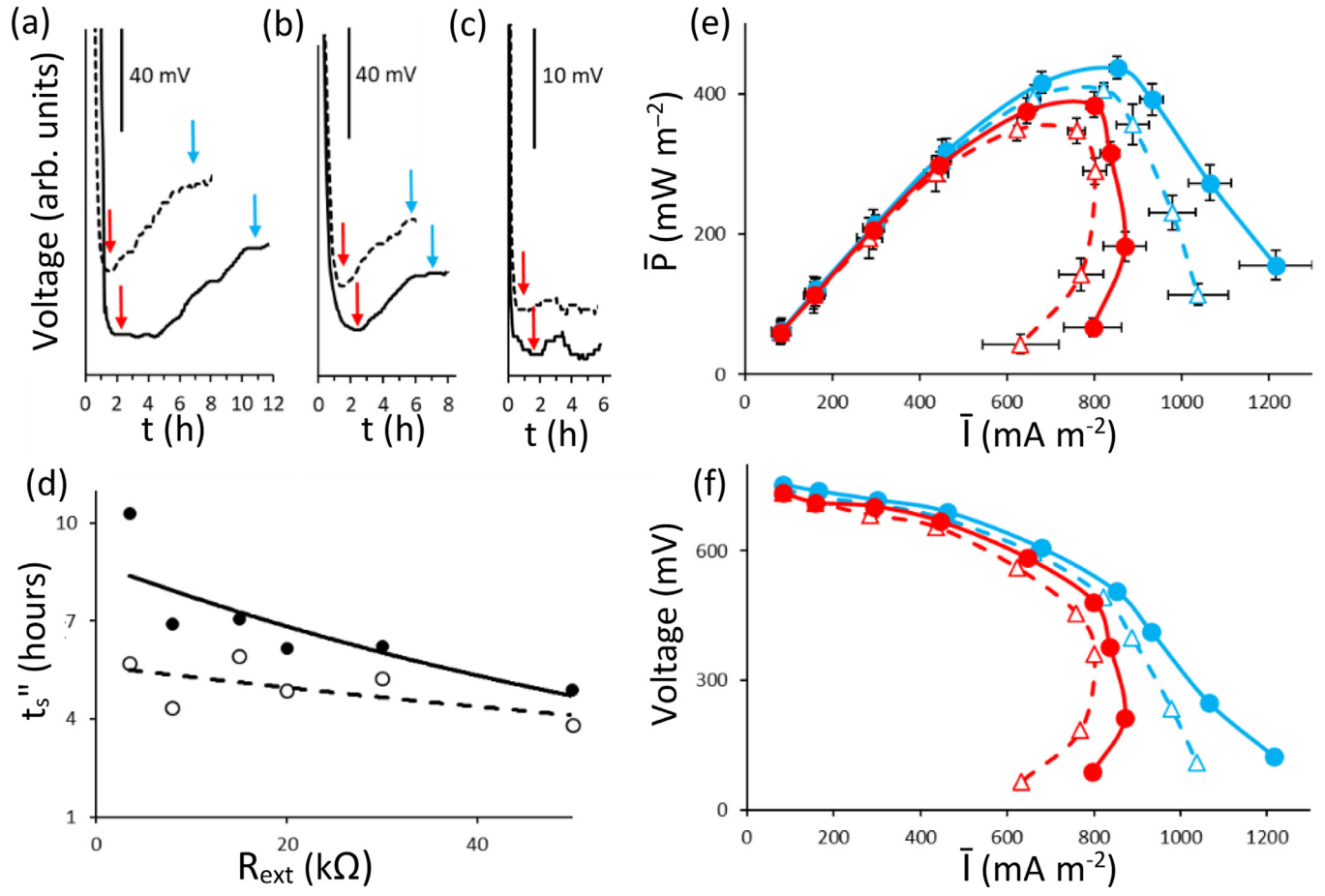

Fig. 5. MFC voltage after switching from OCV to external resistance of (a) 3.5 kΩ, (b) 30 kΩ, and (c) 300 kΩ. Each figure includes results under total flow rates of Q_T=1 mL h^{-1} (solid) and 10 mL h^{-1} (dashed). Arrows in (a), (b) and (c) show the time after reaching the lowest voltage (t_s', red), and (a) and (b) indicate only the acclimation time sufficient to observe full voltage recovery (t_s'' blue). Vertical black scale bars indicate the range corresponding to the marked voltage. (d) Time required to reach the long-term voltage stability (t_s'') versus R_{ext} from 50 kΩ to 3.5 kΩ for total flow rates of Q_T=1 mL h^{-1} (solid) and 10 mL h^{-1} (hollow). For eye guidance, solid and dashed lines indicate exponential fits for Q_T=1 mL h^{-1} and 10 mL h^{-1}, respectively. Reconstructed power density (e) and polarization curves (f) for total flow rates Q_T=1 mL h^{-1} (Δ) and 10 mL h^{-1} (•). Reconstructions were created based on polarization test voltages obtained at time $t = t_s'$ (red curves) and $t = t_s''$ (blue curves). External resistors used were 300, 150, 80, 50, 30, 20, 15, 8, and 3.5 kΩ. Data were obtained between t = 150 and 170 days. Each data point in (e) and (f) is the average of three points, but error bars (standard deviation in average) are shown only for (e).

h^{-1}), even compared to the pre-overshoot values obtained using the standard (non-acclimated) measurement protocol. Increasing the flow rate to Q_T=10 mL h^{-1} had a beneficial effect on $\bar{P}_{max}$ and $\bar{I}_{max}$ ($\bar{P}_{max}$=436 mW m^{-2} and $\bar{I}_{max}$=1215 mA m^{-2}). Made possible by the microfluidic-assisted long-hold approach, in-progress acclimation especially favours higher measurements of $\bar{I}$ at low R_{ext} (including high values of $\bar{I}_{max}$), leading to an unusual shape of the curves in Fig. 5. We do not believe that this shape is an artefact of the technique, but rather, it is the true form of a properly acclimated MFC at each external resistor that enables full long-term biological adaption. This view is supported by the similar $\bar{I}$ values obtained using the 4-day pre-acclimation approach at R_{ext}=3.5 kΩ (before the subsequent standard polarization tests) and from similar power density curve shapes in multi-cycle acclimation conducted in bulk MFCs [10].

We extended the advantage of the long-hold polarization test to construct and investigate power density curves at arbitrary hold times of $t < t_s'$ (i.e., to investigate the effect of polarization tests that were too fast). Power density curves from discharge curves obtained under Q_T=1 mL h^{-1} using virtual hold times of 2 h or less were chosen to mimic standard polarization test conditions used in this work (Supplementary Materials, Section S8). The longest hold time was 2 h ($t \approx t_s'$) and resulted in a power density curve that was nearly identical to the constructed power density curve in Fig. 5e for $t = t_s'$ (Q_T=1 mL h^{-1}). This was expected because 2 h was sufficient to obtain short-term stability in all experiments. This "stable overshoot" does not represent a measurement error because stability was achieved, but it does represent a suboptimal experimental design because it did not account for the voltage recovery after long-term biological stability was reached. A 90 min hold time resulted in a worse overshoot (type D), and a further reduction in the hold time to 60 min caused a drop in power density near the apex of the power density curve, similar to that (type M-like overshoot) observed in Fig. 2a after t = 45 days. Further reductions to virtual hold time resulted in power densities that were unrealistically high. Therefore, we confirm that conducting measurements before short-term reactor stability is reached in a standard polarization test can produce a range of power density curve irregularities. The use of a constant-flow MFC allows for real-time monitoring the voltage discharge during the polarization test to ensure proper long-term biological stability is achieved at each external resistor.

4. Discussion

To summarize the effects on the health-compromised MFC outputs after the applied interventions, we refer to Fig. 6. After shear erosion of the EAB outer layers followed by a restabilization pe-

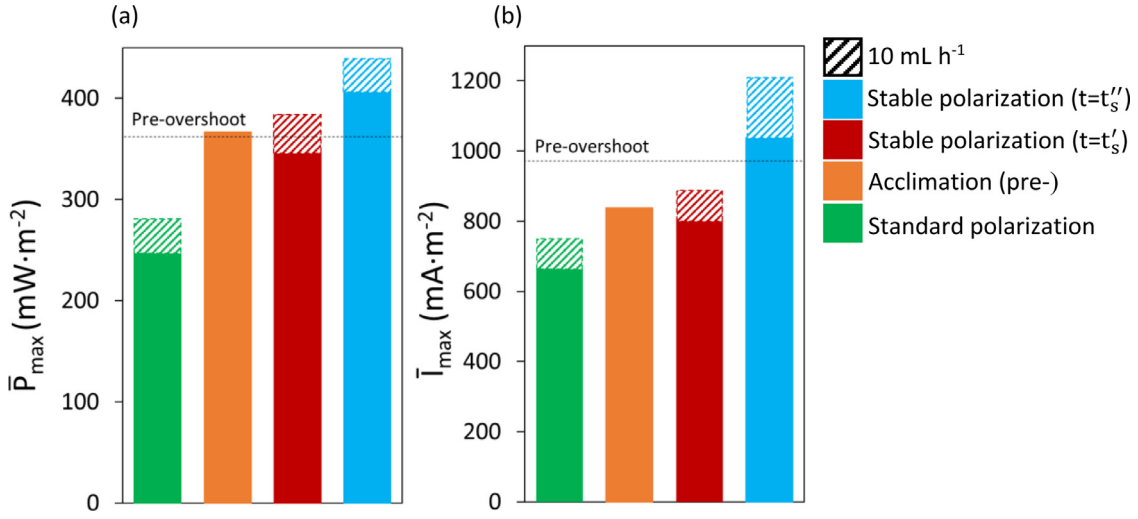

Fig. 6. A summary of the effect of the acclimation methods on (a) maximum power density ($\bar{P}_{max}$) and (b) maximum current density ($\bar{I}_{max}$) following shear erosion at Q_T=1 mL h^{-1} (solid bars) and Q_T=10 mL h^{-1} (cross-hatched bars). The respective pre-overshoot values obtained at t = 42 days are shown as horizontal dashed lines.

riod of 10 days, $\bar{P}_{max}$ and $\bar{I}_{max}$ were much diminished compared to their pre-overshoot values. The power density curve anomaly at 25 kΩ was eliminated after removal of the outer biofilm layer due to a decrease in the settling time to short-term stability during the polarization test discharge profile. Therefore, it is assumed that the outer EAB layers formed an electrical and/or nutrient transport barrier. Two strata are observable from SEM images (Supplementary Materials Section S9). The lower stratum, which contained residual EAB following shear erosion, showed more extracellular polymeric substance possibly as a response to certain physicochemical challeges to the EAB. This may have been related to the higher electron transfer resistance that caused a transition to the underperforming state. The upper stratum contained bacterial cells only (no extracellular polymeric substance), indicating that after shear erosion the EAB regrew without exposure to the abovementioned challenges that may have initially caused EPS production in the lower stratum. Except for some debris, SEM showed that the biofilm was uniform in height and displayed no cracks or crevices, indicating that the shear erosion was experienced evenly everywhere and not through any preferential flow paths. Although it is not shown in Fig. 6, the overshoot persisted after shear erosion but with a reduced $\Delta\bar{I}_{OS}$ (89 mA m^{-2}). Increasing the flow rate to Q_T=10 mL h^{-1} resulted in improvements to all figures of merit, including a further reduced $\Delta\bar{I}_{OS}$ (40 mA m^{-2}). Next, we applied a 4-day pre-acclimation to 3.5 kΩ followed by a standard polarization test. This eliminated overshoot ($\Delta\bar{I}_{OS}$=0) and returned $\bar{P}_{max}$ to pre-overshoot levels, though $\bar{I}_{max}$ still remained lower than the initial (pre-overshoot) levels. Pre-acclimation also produced better performance compared to waiting for short-term stability (at t=t_s') for the same flow rates. Finally, a long-hold polarization test enabled in-progress acclimation until long-term stability was reached during the polarization test ateach R_{ext}. This method maintained $\Delta\bar{I}_{OS}$=0 (no measured overshoot) and a correlated improvement in $\bar{P}_{max}$ and $\bar{I}_{max}$, which even surpassed values obtained using the standard polarization test before the MFC overshoot began. By combining the in-progress acclimation during a long-hold polarization test with an increased flow rate, the measured $\bar{P}_{max}$ and $\bar{I}_{max}$ were further improved. In the absence of any acclimation, the absolute overshoot and MFC performance returned to the previously measured non-acclimated, post-erosion levels. It is important to reiterate that all interventions must be applied to the MFC after reaching steady-state or else the biofim growth will contribute to changes during the measurement. While the long-hold polarization tests may be lengthy, they can provide idealized performance assessment, which future studies may include as a benchmark to compare against standard polarization tests.

Looking towards the future, when the integration of reference electrodes into microfluidic MFCs is more straightforward, we anticipate new studies that include EIS and voltammetry to more deeply investigate overshoot. Based on the observations in this work, it is apparent that the power overshoot was caused by slow electron transfer kinetics. This resulted in the polarization tests being conducted before EAB was adequately stabilized. This is demonstrated by the ability to eliminate overshoot and even improve the measurement results of an underperforming MFC using the long-hold technique compared to the measurements on the initially well-performing EAB using a standard polarization technique. The reader is directed to the Supplementary Materials (Section S10) where we have summarized the terminology, conclusions and guidelines on proper conduction of polarization tests. Future studies using the long-hold polarization test method should be attempted on multispecies EABs, which will likely benefit from more time to adjust population dynamics and other complex responses to changing conditions during the measurement in order to better mimic the long-term operational conditions of the MFC at every applied external resistor. Experiments should also include the application of long-hold polarization on well-performing MFCs to see if benefits can be realized beyond underperforming MFCs. In addition, long-hold measurements should be applied at even lower resistances (approaching short circuit) to determine if overshoot behaviour will eventually be produced and if so, at what values of R_{ext}.

5. Conclusions

A pure-culture *Geobacter sulfurreducens* microfluidic MFC with a membraneless configuration was used to study overshoot behaviour under controlled flow rates. Power overshoot was observed in the power density curves from a standard polarization test when applying different external resistors (from high to low) at cycle times of up to 90 min. The current overshoot is likely related to a slow response from the microbes during adjustment to the new resistances during the polarization test. Eroding the outer EAB layers under strong shear forces improved the power density curve shape, but the overshoot at low resistances persisted. Moderate increases to the flow rate (below erosion levels) reduced the overshoot, but its elimination was only achieved via in-progress accli-

mation during long-hold polarization test. No intervention made could recover the MFC from its underperforming state (based on (i) persistent levels of absolute overshoot in the absence of acclimation, (ii) reduced cell voltage, and (iii) lower current compared to the mature well-performing state), but long-hold polarization tests produced results that were better than the results obtained using the standard polarization test applied to the initially well-performing state. We anticipate that in-progress acclimation could be applied to well-performing MFCs to also obtain measurements results that represent long-term MFC operation. We conclude that underperforming MFCs can cause challenges in properly conducting polarization test, but that long-hold measurement can avoid artifacts such as overshoot in power density curves.

Declaration of Competing Interest

The authors declare that they have no known competing financial interests or personal relationships that could have appeared to influence the work reported in this paper.

Credit authorship contribution statement

Mehran Abbaszadeh Amirdehi: Data curation, Formal analysis, Investigation, Validation, Writing – review & editing. **Lingling Gong:** Investigation, Writing – original draft. **Nastaran Khodaparastasgarabad:** Investigation. **Jayesh M. Sonawane:** Investigation, Writing – review & editing. **Bruce E. Logan:** Funding acquisition, Resources, Writing – review & editing. **Jesse Greener:** Conceptualization, Formal analysis, Funding acquisition, Methodology, Project administration, Resources, Supervision, Writing – review & editing.

Acknowledgements

The authors wish to acknowledge funding agencies Natural Sciences and Engineering Research Council of Canada (NSERC) and Sentinelle Nord for their financial support and Molly K. Gregas for assistance with technical edits.

Supplementary materials

Supplementary material associated with this article can be found, in the online version, at doi:10.1016/j.electacta.2021.139771.

References

[1] D.R. Bond, D.E. Holmes, L.M. Tender, D.R. Lovley, Electrode-reducing microorganisms that harvest energy from marine sediments, Science 295 (2002) 483–485.
[2] B.E. Logan, Microbial Fuel Cells, John Wiley & Sons, 2008.
[3] B.E. Logan, B. Hamelers, R. Rozendal, U. Schröder, J. Keller, S. Freguia, P. Aelterman, W. Verstraete, K. Rabaey, Microbial fuel cells: methodology and technology, Environ. Sci. Technol. 40 (2006) 5181–5192.
[4] P.C. Nien, C.Y. Lee, K.C. Ho, S.S. Adav, L. Liu, A. Wang, N. Ren, D.J. Lee, Power overshoot in two-chambered microbial fuel cell (MFC), Bioresour. Technol. 102 (2011) 4742–4746.
[5] B. Kim, J. An, I.S. Chang, Elimination of power overshoot at bioanode through assistance current in microbial fuel cells, ChemSusChem 10 (2017) 612–617.
[6] S.B. Velasquez-Orta, T.P. Curtis, B.E. Logan, Energy from algae using microbial fuel cells, Biotechnol. Bioeng. 103 (2009) 1068–1076.
[7] J. Winfield, I. Ieropoulos, J. Greenman, J. Dennis, The overshoot phenomenon as a function of internal resistance in microbial fuel cells, Bioelectrochemistry 81 (2011) 22–27.
[8] B. Min, Ó.B. Román, I. Angelidaki, Importance of temperature and anodic medium composition on microbial fuel cell (MFC) performance, Biotechnol. Lett. 30 (2008) 1213–1218.
[9] (a) H.C. B.oghani, J.R. K.im, R.M. D.insdale, A.J. G.uwy, G.C. P.remier, Control of power sourced from a microbial fuel cell reduces its start-up time and increases bioelectrochemical activity, Bioresour. Technol. 140 (2013) 277–285; (b) Y. Hong, D.F. Call, C.M. Werner, B.E. Logan, Adaptation to high current using low external resistances eliminates power overshoot in microbial fuel cells, Biosens. Bioelectron. 28 (2011) 71–76.
[10] V.J. Watson, B.E. Logan, Analysis of polarization methods for elimination of power overshoot in microbial fuel cells, Electrochem. Commun. 13 (2011) 54–56.
[11] H. Rismani-Yazdi, A.D. Christy, S.M. Carver, Z. Yu, B.A. Dehority, O.H. Tuovinen, Effect of external resistance on bacterial diversity and metabolism in cellulose-fed microbial fuel cells, Bioresour. Technol. 102 (2011) 278–283.
[12] D.R. Lovley, T. Ueki, T. Zhang, N.S. Malvankar, P.M. Shrestha, K.A. Flanagan, M. Aklujkar, J.E. Butler, L. Giloteaux, A.E. Rotaru, Geobacter: the microbe electric's physiology, ecology, and practical applications, Adv. Microb. Physiol. 59 (2011) 1–100.
[13] R.M. Snider, S.M. Strycharz-Glaven, S.D. Tsoi, J.S. Erickson, L.M. Tender, Long-range electron transport in Geobacter sulfurreducens biofilms is redox gradient-driven, Proc. Natl. Acad. Sci. 109 (2012) 15467–15472.
[14] Z. Li, A. Venkataraman, M.A. Rosenbaum, L.T. Angenent, A laminar-flow microfluidic device for quantitative analysis of microbial electrochemical activity, ChemSusChem 5 (2012) 1119–1123.
[15] M.P. Zarabadi, M. Couture, S.J. Charette, J. Greener, A generalized kinetic framework applied to whole-cell bioelectrocatalysis in bioflow reactors clarifies performance enhancements for geobacter sulfurreducens biofilms, ChemElectroChem 6 (2019) 2715–2718.
[16] M.P. Zarabadi, S.J. Charette, J. Greener, Toggling Geobacter sulfurreducens metabolic state reveals hidden behaviour and expanded applicability to sustainable energy applications, Sustain. Energy Fuels 3 (2019) 2211–2217.
[17] M.P. Zarabadi, S.J. Charette, J. Greener, Flow-based deacidification of Geobacter sulfurreducens biofilms depends on nutrient conditions: a microfluidic bioelectrochemical study, ChemElectroChem 5 (2018) 3645–3653.
[18] X. Luo, W. Xie, R. Wang, X. Wu, L. Yu, Y. Qiao, Fast start-up microfluidic microbial fuel cells with serpentine microchannel, Front. Microbiol. 9 (2018) 2816.
[19] Y. Yang, D. Ye, J. Li, X. Zhu, Q. Liao, B. Zhang, Microfluidic microbial fuel cells: from membrane to membrane free, J. Power Sources 324 (2016) 113–125.
[20] S. Choi, Microscale microbial fuel cells: advances and challenges, Biosens. Bioelectron. 69 (2015) 8–25.
[21] S. Choi, J. Chae, Optimal biofilm formation and power generation in a micro-sized microbial fuel cell (MFC), Sens. Actuators A Phys. 195 (2013) 206–212.
[22] H. Hou, L. Li, Y. Cho, P. De Figueiredo, A. Han, Microfabricated microbial fuel cell arrays reveal electrochemically active microbes, PLoS ONE 4 (2009) e6570.
[23] W.A. Braff, C.R. Buie, M.Z. Bazant, Boundary layer analysis of membraneless electrochemical cells, J. Electrochem. Soc. 160 (2013) A2056.
[24] M.A. Amirdehi, N. Khodaparastasgarabad, H. Landari, M.P. Zarabadi, A. Miled, J. Greener, A High-performance membraneless microfluidic microbial fuel cell for stable, long-term benchtop operation under strong flow, ChemElectroChem 7 (2020) 2227–2235.
[25] D.F.A.G.E. Boucher, Chemical Engineers' Handbook, 4th Edition, Section 5, 4th Ed., McGraw-Hill, New York, N. Y., 1963 4 Ed..
[26] B.P. Sebastián, D. Schrott Germán, R. Lucianaa, B.J. Pablo, Charge accumulation and electron transfer kinetics in Geobacter sufurreducens biofilms, Energy Environ. Sci. 5 (2012) 6188–6195.
[27] Y. Liu, H. Kim, R. Franklin, D.R. Bond, Gold line array electrodes increase substrate affinity and current density of electricity-producing G. sulfurreducens biofilms, Energy Environ. Sci. 3 (2010) 1782–1788.
[28] K. Lawson, R. Rossi, J.M. Regan, B.E. Logan, Impact of cathodic electron acceptor on microbial fuel cell internal resistance, Bioresour. Technol. 316 (2020) 123919.
[29] C. Moß, N. Jarmatz, D. Hartig, L. Schnöing, S. Scholl, U. Schröder, Studying the impact of wall shear stress on the development and performance of electrochemically active biofilms, Chempluschem 85 (2020) 2298–2307.
[30] G.L. Chadwick, F.J. Otero, J.A. Gralnick, D.R. Bond, V.J. Orphan, NanoSIMS imaging reveals metabolic stratification within current-producing biofilms, Proc. Natl. Acad. Sci. 116 (2019) 20716–20724.
[31] (a) Y. Liu, J.H. Tay, The essential role of hydrodynamic shear force in the formation of biofilm and granular sludge, Water Res. 36 (2002) 1653–1665; (b) J.B. Kaplan, Biofilm dispersal: mechanisms, clinical implications, and potential therapeutic uses, J. Dent. Res. 89 (2010) 205–218.
[32] D. Vigolo, T.T. Al-Housseiny, Y. Shen, F.O. Akinlawon, S.T. Al-Housseiny, R.K. Hobson, A. Sahu, K.I. Bedkowski, T.J. DiChristina, H.A. Stone, Flow dependent performance of microfluidic microbial fuel cells, Phys. Chem. Chem. Phys. 16 (2014) 12535–12543.
[33] M.P. Zarabadi, F.o. Paquet-Mercier, S.J. Charette, J. Greener, Hydrodynamic effects on biofilms at the biointerface using a microfluidic electrochemical cell: case study of *Pseudomonas sp*, Langmuir 33 (2017) 2041–2049.
[34] L.M. Tender, C.E. Reimers, H.A. Stecher, D.E. Holmes, D.R. Bond, D.A. Lowy, K. Pilobello, S.J. Fertig, D.R. Lovley, Harnessing microbially generated power on the seafloor, Nat. Biotechnol. 20 (2002) 821–825.
[35] X. Zhu, J.C. Tokash, Y. Hong, B.E. Logan, Controlling the occurrence of power overshoot by adapting microbial fuel cells to high anode potentials, Bioelectrochemistry 90 (2013) 30–35.
[36] H. Richter, K.P. Nevin, H. Jia, D.A. Lowy, D.R. Lovley, L.M. Tender, Cyclic voltammetry of biofilms of wild type and mutant *Geobacter sulfurreducens* on fuel cell anodes indicates possible roles of OmcB, OmcZ, type IV pili, and protons in extracellular electron transfer, Energy Environ. Sci. 2 (2009) 506–516.
[37] A. Ter Heijne, M. Pereira, J. Pereira, T. Sleutels, Electron storage in electroactive biofilms, Trends Biotechnol. 39 (2021) 34–42.
[38] M.D. Yates, S.M. Strycharz-Glaven, J.P. Golden, J. Roy, S. Tsoi, J.S. Erickson, M.Y. El-Naggar, S.C. Barton, L.M. Tender, Measuring conductivity of living *Geobacter sulfurreducens* biofilms, Nat. Nanotechnol. 11 (2016) 910–913.

[39] N.S. Malvankar, M. Vargas, K.P. Nevin, A.E. Franks, C. Leang, B.-.C. Kim, K. Inoue, T. Mester, S.F. Covalla, J.P. Johnson, Tunable metallic-like conductivity in microbial nanowire networks, Nat. Nanotechnol. 6 (2011) 573–579.
[40] I. Ieropoulos, J. Winfield, J. Greenman, Effects of flow-rate, inoculum and time on the internal resistance of microbial fuel cells, Bioresour. Technol. 101 (2010) 3520–3525.
[41] H.T. Pham, N. Boon, P. Aelterman, P. Clauwaert, L. De Schamphelaire, P. Van Oostveldt, K. Verbeken, K. Rabaey, W. Verstraete, High shear enrichment improves the performance of the anodophilic microbial consortium in a microbial fuel cell, Microb. Biotechnol. 1 (2008) 487–496.
[42] D. Sun, S. Cheng, A. Wang, F. Li, B.E. Logan, K. Cen, Temporal-spatial changes in viabilities and electrochemical properties of anode biofilms, Environ. Sci. Technol. 49 (2015) 5227–5235.
[43] P.S. Jana, K. Katuri, P. Kavanagh, A. Kumar, D. Leech, Charge transport in films of geobacter sulfurreducens on graphite electrodes as a function of film thickness, Phys. Chem. Chem. Phys. 16 (2014) 9039–9046.